# Observation of asymmetric distributions of magnetic singularities across magnetic multilayers

A. Hierro-Rodriguez,[1] C. Quirós,[2,3] A. Sorrentino,[4] C. Blanco-Roldán,[2,3] L. M. Alvarez-Prado,[2,3] J. I. Martín,[2,3] J. M. Alameda,[2,3] E. Pereiro,[4] M. Vélez,[2,3] and S. Ferrer[4]

[1]*Instituto de Física dos Materiais da Universidade do Porto (IN-IFIMUP), Departamento de Física e Astronomia, Faculdade de Ciencias, Universidade do Porto, 4169-007 Porto, Portugal*

[2]*Departamento de Física, Universidad de Oviedo, 33007 Oviedo, Spain*

[3]*Centro de Investigación en Nanomateriales y Nanotecnología (CINN) (Consejo Superior de Investigaciones Científicas (CSIC)—Universidad de Oviedo), 33940 El Entrego, Spain*

[4]*ALBA Synchrotron, 08290 Cerdanyola del Vallès, Spain*

(Received 16 September 2016; revised manuscript received 19 December 2016; published 26 January 2017)

Whereas a great deal of work is being devoted to magnetic singularities in two-dimensional (2D) systems (surfaces, interfaces, films) due to their possible applications, much less is known about their properties along the perpendicular direction. Here, we report on a pronounced asymmetry of the in-depth distribution of meronlike magnetic textures, which are magnetic singularities similar to ½ skyrmions, in magnetic layers. Meron textures are observed to be distributed in two groups defined by their topology. One of them resides almost exclusively at the top surface of the film and the other at the bottom one. This observation has been brought to light with element-specific magnetic transmission soft x-ray microscopy. Micromagnetic simulations reveal that closure domains are at the origin of this asymmetry. The result might be of general interest for controlling magnetic three-dimensional (3D) architectures.

DOI: 10.1103/PhysRevB.95.014430

## I. INTRODUCTION

Magnetic singularities in thin films are a subject of intense research since their stability is appropriate for applications in transport of information in magnetic devices. A variety of magnetic singularities has been investigated, including vortices in magnetic dots [1], half vortices and domain walls in nanowires [2], Bloch points in perpendicular magnetic anisotropy (PMA) materials and nanowires [3,4], or magnetic dislocations [5], and skyrmions in helical magnets [6,7] and multilayers [8–10]. The controlled manipulation of magnetic singularities depends on their topological characteristics as chirality and polarity [11–15] which, in certain cases, can be used to establish detailed procedures for their nucleation [16–19]. Up to now, most of the published research deals with magnetic defects and transport confined in two-dimensional (2D) thin films, i.e. films with magnetization quasiuniform along their thickness. In this paper, we have concentrated on the direction perpendicular to the interfaces since vertical coupling mechanisms are also fundamental for the design of three-dimensional (3D) magnetic devices [20–22]. As it will be described below, a strong asymmetry in the propagation of meronlike magnetic defects across a multilayer film was observed. Depending on their topological characteristics, meronlike textures appear at the upper or lower part of the film. This finding has been rationalized with micromagnetic simulations which revealed that the closure domains that minimize stray fields in the multilayer are the symmetry-selecting agents.

Magnetic merons are topological defects similar to skyrmions but with half of their skyrmionic charge, i.e. the orientation of the magnetization vector covers half of the unit sphere. A variety of merons has been identified in magnetic systems, such as in-plane magnetic vortices [23], or at endpoints of helical or PMA stripes [16,24–29]. In this second case, the magnetic configuration at the stripe endpoint in a 2D magnetic film consists of an in-plane half vortex plus an out-of-plane polarity change (see Fig. 1). According to Ezawa [25], the magnetic configuration at a stripe endpoint in a 2D magnetic film can be considered as an individual magnetic defect since it is physically separated from the other end of the stripe, and its skyrmionic charge, calculated within a half-disk region (dashed line in Fig. 1) covering the stripe endpoint, is $Q = 1/2$. Magnetic domains in PMA films are often organized in arrays of parallel magnetic stripes that frequently show branching and endpoints leading to the so-called magnetic dislocations where meronlike magnetic textures as in Fig. 1 are sometimes formed [28]. Exchange and magnetostatic interactions may lead to the propagation of these textures across the thickness in 3D multilayers.

In this paper, we report on the description of meronlike magnetic textures in multilayers consisting of a thin weak PMA layer sandwiched in between two in-plane anisotropy magnetic layers and on the observed asymmetries in the distribution of these magnetic singularities across the multilayer thickness. The results are based on detailed imaging of the domains with a soft x-ray microscope. The relatively large probing depth (more than 100 nm) and the atom-specific magnetic dichroic images acquired at different angles allowed us to show that the top and bottom surfaces of the films present meronlike textures with different topological characteristics. This finding has been rationalized with two selection rules which might be of general use for the control of 3D magnetic architectures.

## II. EXPERIMENTAL

### A. Sample preparation

Magnetic configuration was studied in $Gd_{12}Co_{88}$/$Nd_{16}Co_{84}$/$Ni_{80}Fe_{20}$ trilayers [Fig. 2(a)] grown on 50-nm-thick $Si_3N_4$ membranes by dc magnetron sputtering from Gd-Co, Nd-Co, and Ni-Fe targets [28,30]. The central Nd-Co

 

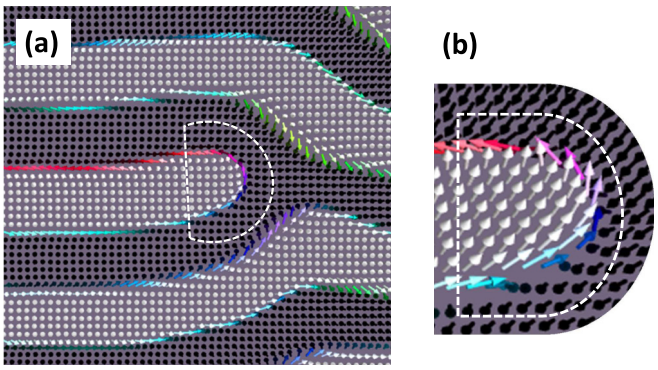


FIG. 1. (a) Magnetization configuration around a dislocation meron within the stripe domain pattern. (b) Zoom of the meron texture localized at the white stripe domain endpoint: Dotted line indicates the stripe endpoint region in which the skyrmionic charge is concentrated; the magnetization contains an in-plane half vortex together with an out-of-plane polarity change—white/black arrows—and, therefore, wraps half of the unit sphere.

layer supports a stripe domain pattern with a typical stripe pattern period $\Lambda$ in the 100–300 nm range [31] that is imprinted by exchange and magnetostatic interactions to the adjacent in-plane anisotropy Gd-Co and Ni-Fe layers. Different magnetic elements are chosen for each layer to allow for an independent mapping of the magnetization at different sample depths using element selective x-ray dichroic absorption [32]. The bottom layer is made of $Gd_{12}Co_{88}$, a ferrimagnetic alloy [30] with saturation magnetization $M_S = 6 \times 10^5$ A/m and in-plane uniaxial anisotropy. At this composition and room temperature, the alloy magnetization is aligned with the

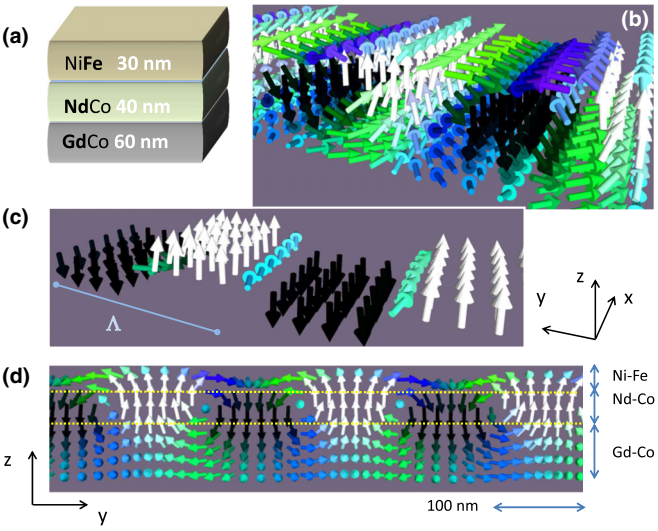


FIG. 2. (a) Trilayer structure (sample A). (b) Micromagnetic simulation of the magnetization of the weak stripe pattern in sample A at remanence. (c) Magnetization configuration at the center of the Nd-Co layer in (b). $\Lambda$ indicates stripe pattern period. Note that, in this central plane, the magnetization is fully out of plane except at the domain walls separating up/down stripes. (d) Magnetization configuration across the thickness in (b). Note the presence of $M_y$-$M_z$ closure domain vortices of alternating chirality.

Co sublattice and antiparallel to the Gd ion magnetization [30]. The central layer is made of $Nd_{16}Co_{84}$, an amorphous ferromagnetic alloy [31] with $M_S = 7.5 \times 10^5$ A/m and weak PMA (out-of-plane anisotropy $K_N = 10^5$ J/m$^3$). The $Ni_{80}Fe_{20}$ permalloy layer has $M_S = 8.5 \times 10^5$A/m and small in-plane uniaxial anisotropy. In-plane easy axes in bottom/top layers are parallel due to sample-target geometry during growth and define $x$ axis direction in the magnetic measurements.

Two trilayers were used in this paper: Sample A (60 nm $Gd_{12}Co_{88}$/40 nm $Nd_{16}Co_{84}$/30 nm $Ni_{80}Fe_{20}$) and sample B (40 nm $Gd_{12}Co_{88}$/60 nm $Nd_{16}Co_{84}$/40 nm $Ni_{80}Fe_{20}$). In order to favor the nucleation of meronlike textures that occurs during in-plane magnetization reversal of the stripe pattern [28], the samples were prepared following different magnetic histories prior to magnetic transmission x-ray microscopy (MTXM) measurements: Sample A was saturated with an in-plane field $\mu_0 H_x = 150$ mT and, then, brought to remanence through several minor loops of decreasing amplitude. Sample B was first saturated with $\mu_0 H_x = -150$ mT; then a small positive field $\mu_0 H_x = 8$ mT was applied to initiate the reversal process (smaller than coercivity $\mu_0 H_x = 10$ mT), and subsequently $\mu_0 H_x$ was reduced to zero. Both samples were imaged at remanence.

### B. MTXM

Samples A and B were imaged at zero field by the full field transmission soft x-ray microscope of the Mistral Beam line at ALBA Synchrotron described elsewhere [28,33,34]. Element-specific magnetic dichroic images were acquired by tuning the circularly polarized photon beam energy to the Fe $L_3$ (706.8 eV), Nd $M_4$ (1000.3 eV), and Gd $M_5$ (1189.6 eV) atomic absorption edges in order to probe the magnetization of top, central, or bottom layers, respectively, which allowed us to image the magnetic domains at the upper, central, and lower part of the multilayer.

The magnetic sensitivity was achieved by selecting photons emitted below the plane of the orbit of the electrons. As the electrons in the storage ring circulate in a clockwise (CW) sense, as seen from above the accelerator, our photon beam was right-handed (RH) circularly polarized (estimated 96% of circular polarization) with angular momentum of the photons in the same sense as the x-ray beam wave vector. The trilayers were mounted on a goniometer, located inside the microscope vacuum chamber, having a vertical rotation axis that was positioned to coincide with the planes of the sample surfaces. At oblique incidence, $\theta$ was defined as the angle between the x-ray beam and the film normal with positive $\theta$ sample rotation angles corresponding to CW rotations, as seen from above the sample. Single images were acquired by exposing the film to the beam during 5 to 40 s, and averages of 4 to 40 images were collected depending on transmission signal statistics which was determined by the layer thickness and the angle of incidence of the beam. The averaged images were normalized to the incoming photon flux, and the background inhomogeneities were corrected by a flat field image, taken without sample. Some of the images were Fourier filtered to remove long spatial frequency experimental artifacts. Stability of the microscope, photon beam, and beamline optics were mandatory for not having blurring and drifts of

the images. The observed magnetic textures were stable for hours.

### C. Micromagnetic simulations

Micromagnetic simulations of the magnetization reversal of 3D GdCo/NdCo/NiFe multilayers were performed for comparison with the MTXM images using the finite difference code MuMax$^3$ for calculations [35] and MuView code [36] for visualization. The films were discretized into cells with dimensions (height × width × depth) of $4 \times 4 \times 4\,\text{nm}^3$ for a total of $4096 \times 4096 \times 128\,\text{nm}^3$. Material parameters for each layer, taken from the magnetic characterization by hysteresis loops of single layers of each material, are (a) permalloy (Ni-Fe): $M_S = 8.5 \times 10^5$ A/m, in plane uniaxial anisotropy $K_u = 850\,\text{J/m}^3$; (b) Nd-Co: $M_S = 7.5 \times 10^5$ A/m and out-of-plane anisotropy $K_N = 1.4 \times 10^5\,\text{J/m}^3$; and (c) Gd-Co: $M_S = 6 \times 10^5$ A/m, $K_u = 4.6 \times 10^3\,\text{J/m}^3$. The corresponding exchange constants are: $A_{EX}$(Ni-Fe) $= 1.3 \times 10^{-11}$ J/m [35], $A_{EX}$(Nd-Co) $= 0.7 \times 10^{-11}$ J/m [28], and $A_{EX}$(Gd-Co) $= 1.0 \times 10^{-11}$ J/m [30].

Figures 2(b)–2(d) show the simulated magnetic configuration of sample A at remanence after saturating with $\mu_0 H_x = 1$ T: in the central Nd-Co layer [Fig. 2(c)], there is a pattern of up and down parallel stripes ($M_z = \pm M_S$) with period $\Lambda$ separated by Bloch walls in which the magnetization is oriented along $M_x$. This periodic pattern is imprinted into the top/bottom layers as a periodic oscillation of the magnetization with smaller $M_z$ amplitude and larger average $M_x$. In addition, a periodic closure domain structure of $M_y$-$M_z$ vortices of alternating rotation sense appears across the sample thickness [Fig. 2(d)].

## III. ANALYSIS OF MAGNETIC CONFIGURATION FROM MTXM IMAGES

Figure 3 shows a series of images of the same region of sample A taken at Fe (top layer), Nd (central layer), and Gd (bottom layer) absorption edges at normal incidence [Figs. 3(a)–3(c)] and at oblique incidence $\theta = 35°$ [Figs. 3(d)–3(f)]. At oblique incidence, $\theta$ is the angle between the x-ray beam and the film normal and x rays are arriving from negative $x$. Magnetic contrast is proportional to the projection of the local magnetization to the x-ray beam direction [32]; thus, the first three images [Figs. 3(a)–3(c)] are only sensitive to $M_z$. They display an identical pattern of black-white stripes with period of ∼250 nm. The same magnetic dislocations (i.e. stripe bifurcations) appear in all the images [the Y1 bifurcation in Fig. 3(b) is not observed due to instrumental reasons described in the figure caption], confirming that the stripe pattern of Nd-Co has been imprinted into the top Ni-Fe and bottom Gd-Co layers. There is just a noticeable difference in Fig. 3(c) in comparison with Figs. 3(a)–3(b): white bifurcations in the Fe and Nd edges appear as black bifurcations in the Gd edge. This contrast reversal is due to the ferrimagnetic character of the Gd-Co alloy at this composition [30]: Gd magnetic moment is antiparallel to Co and to the net magnetization vector at each point which leads to this reversal in magnetic contrast. The precise relationship of the contrasts of the images and the signs of the magnetization was

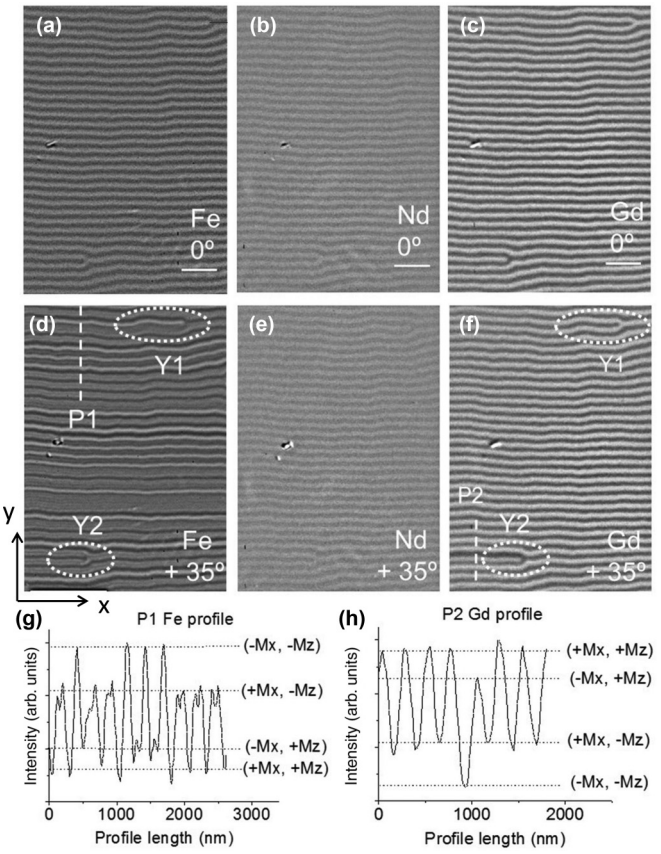


FIG. 3. (a)–(c) Magnetic domains in sample A of the same region acquired at $\theta = 0°$ ($M_z$ contrast). (a), (b), and (c) correspond to Fe (top Ni-Fe layer), Nd (central Nd-Co layer), and Gd (bottom Gd-Co layer) magnetizations, respectively. Scale bar 1 $\mu$m. Images (d)–(f) are from the same area acquired at $\theta = 35°$: they include $M_x$ and $M_z$ contrast and are contracted by a factor $1/\cos(35°) = 1.22$ along the $x$ direction. Note the differences in contrast around dislocations Y1 and Y2 between the images (d) and (f) corresponding to top/bottom layers, respectively. (g) and (h) Contrast profiles at $\theta = 35°$ along P1 and P2 lines on images (d) and (f). The four contrast levels arise from the different ($M_x$,$M_z$) sign combinations. Note that dislocation Y1 is out of the field of view in (b) due to a 0.5 $\mu$m horizontal displacement of this image relative to (a) and (c).

determined from the handedness of the x-ray helicity and the sample geometry: [black, white] corresponds to $[+M_z, -M_z]$ in Figs. 3(a)–3(b), whereas [white, black] to $[+M_z, -M_z)$ in Fig. 3(c).

Figures 3(d)–3(f), measured at $\theta = 35°$, include both $M_x$ and $M_z$ contrast due to the oblique x-ray incidence. A fact is very clear at the Fe edge image [Fig. 3(d)]: the stripe pattern now contains four levels of gray that correspond to $[(+M_x, +M_z),(-M_x, +M_z),(+M_x, -M_z),(-M_x, -M_z)]$ domains, respectively, as indicated by the intensity profiles in Fig. 3(g). Taking into account x-ray photon polarization and the microscope geometry, it is possible to extract unequivocally the local orientation of $M_x$ and $M_z$ in each of the three layers from the absorption intensities and their variation with $\theta$ angle. In more detail, for Fe $L_3$ and Nd $M_4$ edges, as absorption is larger (smaller) for parallel (antiparallel) alignment between the angular momentum of

the photons and the sample magnetization [32], white (black) stripes correspond to negative (positive) signs of $M_z$. In addition, at positive $\theta$ angles, brighter (darker) white stripes correspond to negative (positive) sense of $M_x$, and darker (less dark) black stripes correspond to positive (negative) $M_x$ sense. For the Gd $M_5$ case, the total magnetization of the GdCo alloy is opposite to the orientation of the Gd magnetic moments [30], and the above rules are sign reversed [Fig. 3(h)].

A meronlike texture can be identified at the upper part of Fig. 3(d) (labeled as Y1): there is a black stripe bifurcation in which one of the branches is black and the other is dark gray. That is, at the dislocation core, $M_x$ performs a $\pi$ rotation (an in-plane half vortex), while $M_z$ is reversed, which corresponds to a meronlike magnetic texture, similar to the sketch in Fig. 1 [25,28]. However, since $M_z$ is smaller than $M_S$ at the top/bottom layers (as shown by micromagnetic simulations in Fig. 2), its skyrmionic charge is in fact smaller than ½, and therefore, it is not a fully developed meron. Here, Nd magnetization images appear very similar at normal and oblique incidence [Figs. 3(b) and 3(e)], indicating a very small in-plane magnetization component at the central layer consistent with the micromagnetic simulations in Fig. 2(c). Also, at the bottom Gd-Co layer, [Fig. 3(f)], an almost uniform stripe pattern is found, quite different from the image of the top Fe-Ni layer. There is just one black stripe at the lower part of the image, corresponding to a $(-M_x,-M_z)$ domain, i.e. an $M_x$ reversed stripe starting at a dislocation core that marks the presence of a meronlike texture (labeled as Y2). Note that contrast reversal at meron Y1 appears only at the top Ni-Fe layer [Fig. 3(d)] but not at the bottom Gd-Co layer [Fig. 3(f)]. On the other hand, meron Y2 is only seen at the Gd image, and no in-plane contrast reversal is found at the Fe image. A statistical analysis of magnetic singularities in the sample shows that the asymmetric in-depth magnetization configuration of meronlike textures bound to dislocations observed in Fig. 3 is a general trend: measurements of 28 different $10 \times 10\ \mu m^2$ sample regions showed that 85% of the observed merons were located either at the top Ni-Fe layer or at the bottom Gd-Co layer but not on both.

Further insight into the origin of these top-bottom magnetization asymmetries can be obtained from the topological characteristics of meron textures in each layer: Burgers vector **B** of the stripe dislocation, polarity $P$, chirality of in-plane half vortex, and $M_x$ sign before bifurcation.

Figure 4 shows two examples illustrating the parameters used to describe the meron textures, taking into account the equivalence between contrast levels and $(M_x,M_z)$ orientation. Figure 4(a) corresponds to a meron texture observed only on the top Fe image but not at the bottom Gd side. First, Burgers vector is determined by the orientation of the bifurcation relative to spatial coordinates: in this case, $\mathbf{B} = \Lambda\,\mathbf{u_y}$ [Fig. 4(a2)] and it will be labeled as B+; second, meron polarity $P$ is given by $M_z$ sign reversal: in this case $M_z$ is pointing up inside the dislocation core so we describe it as P+ [Fig. 4(a3)]; third, chirality of meron in-plane half vortex is given by the rotation sense of $M_x$ in the reversed/unreversed stripes after the bifurcation: CW in this case [Fig. 4(a4)]; finally, $M_x$ orientation before the bifurcation is negative in this case, and it will be labeled as $M_x-$ [Fig. 4(a4), arrow at

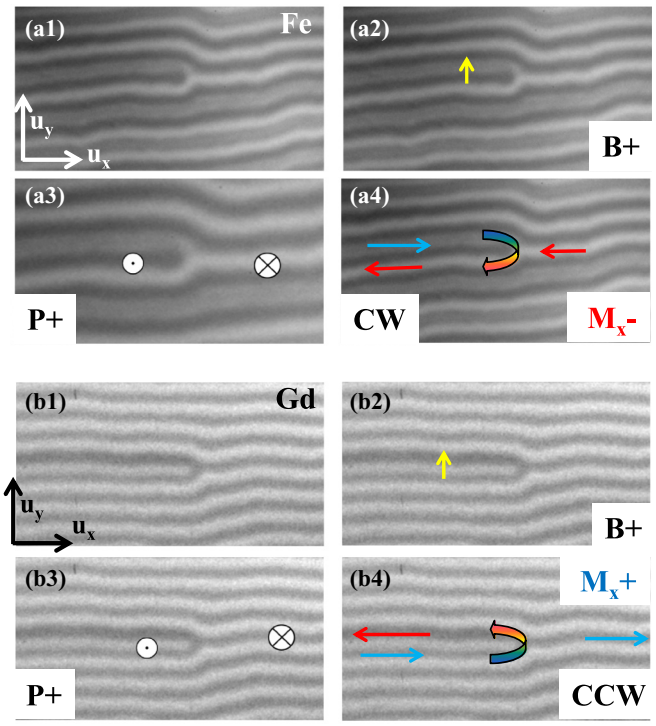


FIG. 4. Definition of parameters used to describe the topology of meronlike textures: (a) Meron texture on the upper layer (Fe magnetization) at $\theta = +35°$: (a1) As measured, (a2) dislocation Burgers vector, (a3) core polarity, and (a4) in-plane half vortex chirality and $M_x$ sign. (b) Same as in (a) for a meron at the bottom layer (Gd magnetization). The overall contrast sign reversal is due to the ferrimagnetic nature of Gd-Co.

TABLE I. Statistics of the observed distribution of meronlike textures in samples A and B. Data are shown for the top Ni-Fe or bottom Gd-Co layers in terms of their topological characteristics: $M_x$ sign, Burgers vector, polarity, and in-plane half vortex chirality.

| | Strong rule | | | | | Weak rule | |
|---|---|---|---|---|---|---|---|
| Sample A | Top NiFe | | | | | | |
| | $M_x+$ | | $M_x-$ | | | | |
| | B+ | B− | B+ | B− | | $M_x+$ | $M_x-$ |
| P+ | 0 | 7 | 2 | 0 | CCW | 4 | 1 |
| P− | 9 | 0 | 0 | 1 | CW | 12 | 2 |
| | Bottom GdCo | | | | | | |
| P+ | 1 | 0 | 0 | 0 | CCW | 2 | 0 |
| P− | 0 | 1 | 0 | 0 | CW | 0 | 0 |
| Sample B | Top NiFe | | | | | | |
| | $M_x+$ | | $M_x-$ | | | | |
| | B+ | B− | B+ | B− | | $M_x+$ | $M_x-$ |
| P+ | 0 | 0 | 149 | 0 | CCW | 0 | 193 |
| P− | 0 | 0 | 0 | 175 | CW | 0 | 131 |
| | Bottom GdCo | | | | | | |
| P+ | 0 | 0 | 0 | 16 | CCW | 0 | 29 |
| P− | 0 | 0 | 14 | 0 | CW | 0 | 1 |

TABLE II. Resulting meron statistics after applying the equivalence between topological indexes by symmetry relations. RH and LH indicate handedness of the Bloch point that has propagated away from the dislocation, deduced from meron chirality and polarity.

| | | $M_x$+,B+,P+ | $M_x$+,B−,P+ | CW | CCW |
|---|---|---|---|---|---|
| Sample A | Top | 0 | 10 | 14(RH) | 5(LH) |
| | Bottom | 11 | 0 | 0(LH) | 2(RH) |
| Sample B | Top | 0 | 163 | 131(RH) | 193(LH) |
| | Bottom | 191 | 0 | 1(LH) | 29(RH) |

the right]. A similar analysis of a meron texture appearing only at the Gd image (i.e. only at the bottom Gd-Co layer) is shown in Fig. 4(b) resulting in [$M_x$+,B+,P+, counterclockwise (CCW)] topological indices.

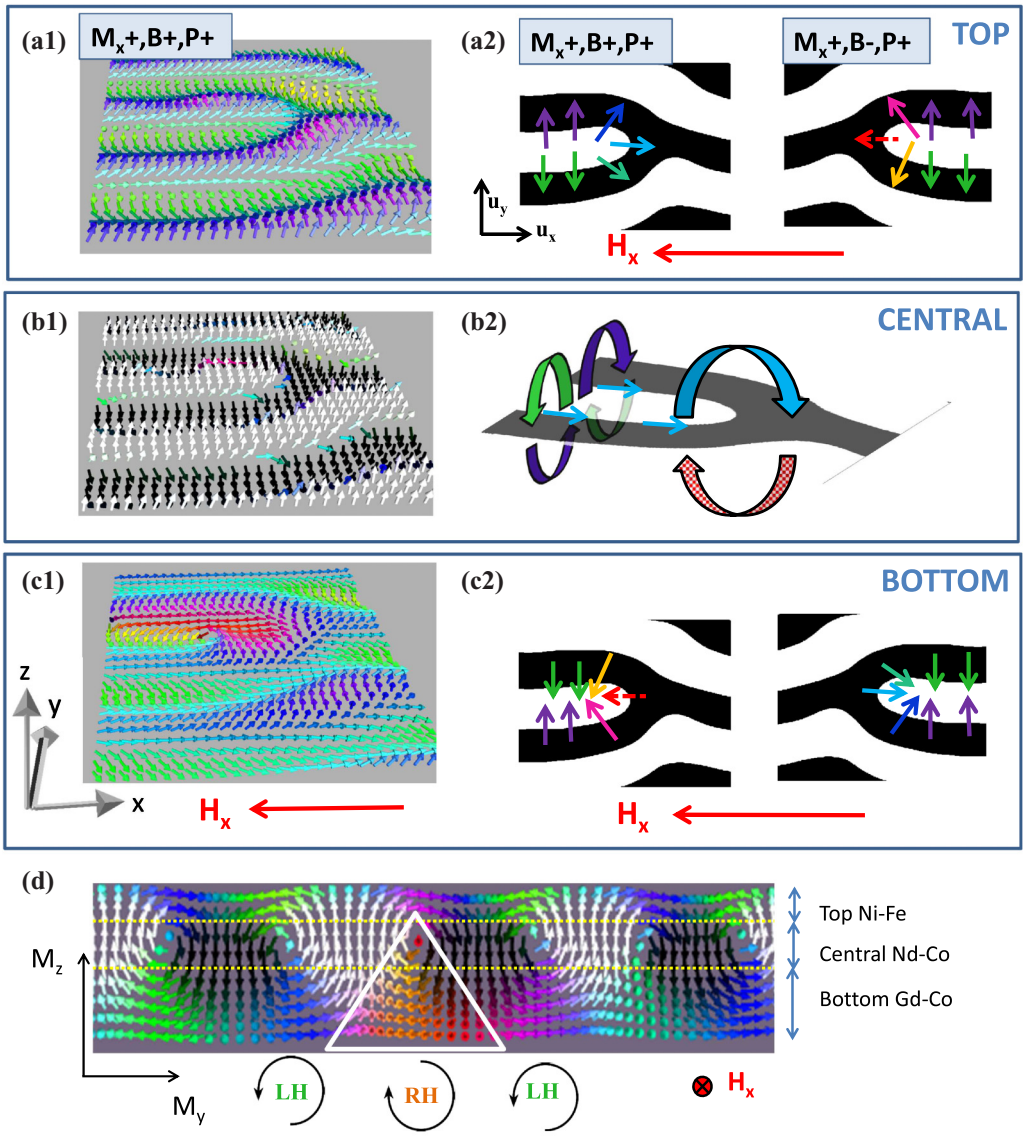


FIG. 5. Micromagnetic configuration at magnetic dislocations (stripe bifurcations) in a 60 nm Gd-Co/40 nm Nd-Co/30 nm Ni-Fe trilayer at (a) top, (b) central, and (c) bottom layers; (a1), (b1), and (c1) micromagnetic simulations; (a2), (b2), and (c2) sketches of ($M_x$,$M_y$) configuration at closure domains around a dislocation core. Note the presence of small $-M_x$ regions at the dislocation core at either top/bottom layers depending on Burgers vector and polarity (see dotted arrows). $H_x$ denotes the field applied to reverse the magnetization of the sample and induce meron texture nucleation (but absent during the MTXM measurements at remanence). (d) Cross-section view of magnetization configuration in a [$M_x$+,B+,P+, CCW, bottom] meron texture obtained by micromagnetic simulations. LH and RH are defined by the hand used to describe closure vortex rotation relative to applied field. White triangle marks the reversed domain at the bottom part of the sample.

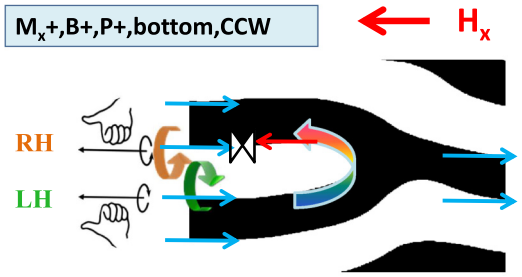


FIG. 6. Sketch indicating the relation between Bloch point handedness (RH/LH) and chirality for a CCW meron texture emerging at bottom side of the film under $-H_x$ field.

## IV. MERON DISTRIBUTION AND MICROMAGNETIC CONFIGURATION

Table I summarizes the topological characteristics of the meron textures observed in samples A and B, either at the Ni-Fe top layer or at the Gd-Co bottom layer. A strong trend (that we will designate as "strong rule" hereafter) is found for certain preferred combinations of $M_x$ sign, Burgers vector, and polarity at each layer, as observed in the left part of Table I. For positive $M_x$, meron textures with (B−,P+) and (B+,P−) appear only at the top Ni-Fe layer, whereas meron textures with (B−,P−) and (B+,P+) emerge only at the bottom side of the sample (Gd-Co layer). For negative $M_x$, this trend is reversed and (B−,P−) and (B+,P+) meron textures are seen only at the top Ni-Fe layer.

A weaker but clear trend may be observed at the right part of Table I regarding in-plane half vortex chirality: in sample A, most meron textures observed at top Ni-Fe layer rotate CW (74%), independently of $M_x$ sign, Burgers vector or polarity; whereas the two meron textures observed at the bottom Gd-Co layer rotate CCW. In Sample B, CCW chirality is dominant at the bottom layer, but CW/CCW distribution is more balanced at the top NiFe layer.

There is also an imbalance in $M_x+/M_x-$ populations that is related to the different magnetic history in each sample. Here, $M_x+$ meron textures dominate in sample A (saturated in a positive $H_x$ field), but there is also a significant number of $M_x-$ meron textures due to the alternating field used in the demagnetization process. In sample B, only $M_x-$ meron textures are observed, which is consistent with its magnetic history: after saturating it with $\mu_0 H_x = -150\,\mathrm{mT}$, magnetization reversal was initiated with a positive field $\mu_0 H_x = 8\,\mathrm{mT}$, smaller than sample coercivity.

The statistical distribution of meron textures in Table I can be simplified considering symmetry operations that result in equivalent magnetization configurations (see Appendix A for details), as shown in Table II. For both studied samples, the strong selection rule is clearly fulfilled, and the analysis of the preferred combinations of topological indices is reduced to a simple question: Why are ($M_x$+,B−,P+) meron textures at the top of the trilayer and ($M_x$+,B+,P+) meron textures at the bottom?

The answer to this question can be traced back to the closure domain structure that develops across the thickness of the stripe pattern due to the stray field of the central layer. This can be illustrated with the micromagnetic simulations of a ($M_x$+,B+,P+) meron texture in a GdCo/NdCo/FeNi trilayer under a negative $H_x$ field that reverses the initially saturated positive $M_x$ magnetization, as shown in Fig. 5. In a parallel stripe domain pattern, the magnetization turns across the thickness in a series of $M_z$-$M_y$ vortices surrounding the $M_x$ Bloch walls that separate stripe domains [see sketch in Fig. 5(b2)]. The strong selection rule originates from the disruption of this periodic closure vortex pattern at stripe domain dislocations. As sketched in Fig. 5(b2), the Bloch wall that bounds the central white stripe locally rotates at the dislocation core from $\mathbf{u_x}$ into the $\mathbf{u_y}$ direction. In turn, the closure domain vortices that surround this Bloch wall rotate from the $M_y$-$M_z$ plane into the $M_x$-$M_z$ plane [see Figs. 5(a2)–5(c2)], and therefore, a small $M_x$ reversed region appears at the dislocation core (see dotted arrows) at top for a (B−,P+) dislocation [Fig. 5(a2)] and at the bottom surface for a (B+,P+) dislocation [Fig. 5(c2)]. As the negative $H_x$ field increases, these reversed regions serve as starting points of in-plane magnetization reversal by the propagation of a Bloch point away from the dislocation core forming a meronlike texture [28]. In this process, a $-M_x$ domain is created confined either to the bottom/top half of the sample depending on the

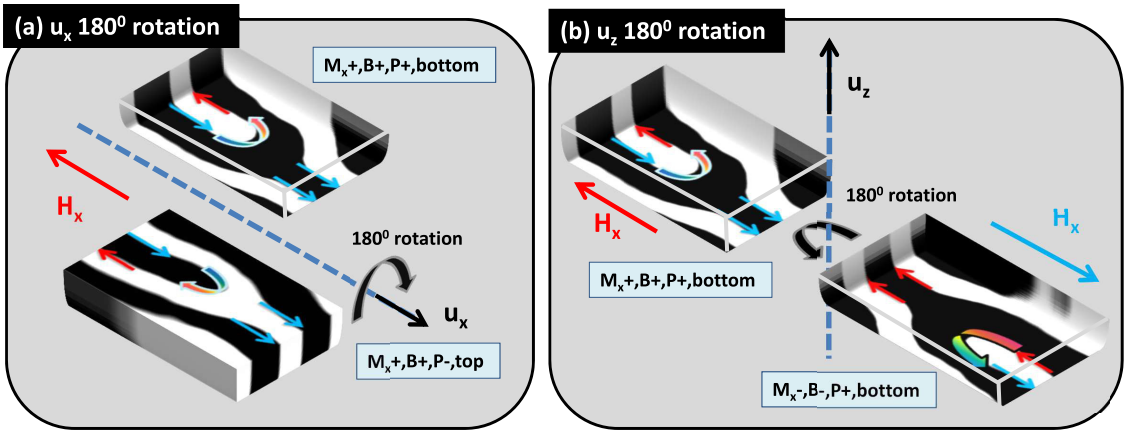


FIG. 7. Transformation of dislocation/meron texture under: (a) a 180° rotation around $\mathbf{u_x}$ showing the reversal of polarity, chirality, and top/bottom exchange; (b) 180° rotation around $\mathbf{u_z}$ showing the reversal of $M_x$ and Burgers vector.

TABLE III. Equivalence relations under 180° rotations around $\mathbf{u_z}$ or $\mathbf{u_x}$ of meronlike textures in sample A. Bold indicates index transformation upon rotation.

| Meron class | $\mathbf{u_z}$180° rotation | $\mathbf{u_x}$180° rotation | $\mathbf{u_z}$180° rotation + $\mathbf{u_x}$180° rotation | Total |
|---|---|---|---|---|
| $M_x$+,B+,P+, top | $M_x$−,**B**−,P+, top | $M_x$+,B+,**P**−, **bottom** | $M_x$−,**B**−,**P**−, **bottom** | |
| 0 | 0 | 0 | 0 | 0 |
| $M_x$+,B+,P+, bottom | $M_x$−,**B**−,P+, bottom | $M_x$+,B+,**P**−, **top** | $M_x$−,**B**−,**P**−, **top** | |
| 1 | 0 | 1 | 1 | 11 |
| $M_x$+,B−,P+, top | $M_x$−,**B**+,P+, top | $M_x$+,B−,**P**−, **bottom** | $M_x$−,**B**+,**P**−, **bottom** | |
| 7 | 2 | 1 | 0 | 10 |
| $M_x$+,B−,P+, bottom | $M_x$−,**B**+,P+, bottom | $M_x$+,B−,**P**−, **top** | $M_x$−,**B**+,**P**−, **top** | |
| 0 | 0 | 0 | 0 | 0 |

location of the initial reversed nucleus [see triangular region at the cross-section depicted in Fig. 5(d) for ($M_x$+,B+,P+) meronlike texture]. Thus, the unbalanced in-depth distribution of meronlike textures is directly related to the opposite in-plane magnetization orientation of closure domains at opposite film surfaces: e.g. for the ($M_x$+,B+,P+) dislocation depicted in Fig. 5, $M_x$ reversal is hindered at the top film surface due to the extra $+M_x$ component of the closure vortex, while it is favored at the bottom surface by the $-M_x$ component of this same closure domain vortex (dotted arrow) in Fig. 5(c2). Inverting Burgers vector moves this small $-M_x$ region at the dislocation core from the bottom to the top sample surface [see e.g. the comparison between ($M_x$+,B+,P+) and ($M_x$+,B−,P+) dislocations sketched in Figs. 5(a2)–5(c2)], in agreement with the strong selection rule experimentally found in Tables I and II. This mechanism relies only on the rotation sense of closure vortices relative to dislocation cores, and therefore, it is independent of the particular materials used in this paper (that were chosen only to have x-ray element selectivity in the different layers), and it is also observed in micromagnetic simulations of NdCo/NiFe bilayers (see Appendix B).

The origin of the second rule, namely the statistical imbalance between CW and CCW meron textures at the upper and lower sides of the film, is more subtle. It can be related to the mechanism for meron texture nucleation at the central Nd-Co layer that requires the propagation of a Bloch point away from the dislocation core along one of the domain walls that bound the stripe domain bifurcation (see sketch in Fig. 6). Depending on the bifurcation branch chosen for Bloch point propagation, the in-plane half vortex chirality of the resulting meronlike texture will be either CW or CCW. As indicated in Fig. 6, the two branches of a magnetic dislocation have different handedness [37], RH and left hand (LH), with respect to the direction of the applied field $H_x$. A possible explanation for the observed CW/CCW imbalance might be the following: The $H_x$ field exerts a gyromagnetic torque on the positive $z$ component of the core magnetization (P+) directed towards the positive $y$ direction that favors the RH branch for the head-to-head Bloch point propagation resulting in a CCW texture. The same argument holds for CW textures at the upper side and P− polarity.

The analysis of the closure vortex handedness in each of the observed meron textures, summarized in Table II, shows that RH Bloch propagation is dominant in sample A at the top and bottom surfaces and in sample B at the bottom surface (97% RH vs 3% LH). However, the top surface of sample B exhibits a more balanced distribution with preference for LH Bloch points (40% RH vs 60% of LH). This different trend might be related to the much larger density of dislocations and meron textures in sample B (0.26 dislocation/$\mu$m$^2$ in comparison with 0.014 dislocation/$\mu$m$^2$ in sample A). Micromagnetic simulations, shown in Appendix B, suggest that interactions between dislocations provide an extra random mechanism for the selection of meron chirality that might explain why the second rule is less robust than the first one.

## V. CONCLUSIONS

In summary, the micromagnetic configurations of meronlike textures bound to magnetic dislocations (i.e. bifurcations in the stripe pattern) in NdCo films sandwiched between GdCo and NiFe layers (over 100 nm total thickness) have been imaged with soft x-ray microscopy by individually mapping the top, central, and bottom parts of the films. Depending on their topological characteristics, meronlike textures are observed almost exclusively at the top or bottom layers.

TABLE IV. Equivalence relations under 180° rotations around $\mathbf{u_z}$ or $\mathbf{u_x}$ of meronlike textures in sample B. Bold indicates index transformation upon rotation.

| Meron class | $\mathbf{u_z}$180° rotation | $\mathbf{u_x}$180° rotation | $\mathbf{u_z}$180° rotation + $\mathbf{u_x}$180° rotation | Total |
|---|---|---|---|---|
| $M_x$+,B+,P+, top | $M_x$−,**B**−,P+, top | $M_x$+,$B$ + ,**P**−, **bottom** | $M_x$−,**B**−,**P**−, **bottom** | |
| 0 | 0 | 0 | 0 | 0 |
| $M_x$+,B+,P+, bottom | $M_x$−,**B**−,P+, bottom | $M_x$+,$B$ + ,**P**−, **top** | $M_x$−,**B**−,**P**−, **top** | |
| 0 | 16 | 0 | 175 | 191 |
| $M_x$+,B−,P+, top | $M_x$−,**B**+,P+, top | $M_x$+,$B$−,**P**−, **bottom** | $M_x$−,**B**+,**P**−, **bottom** | |
| 0 | 149 | 0 | 14 | 163 |
| $M_x$+,B−,P+, bottom | $M_x$−,**B**+,P+, bottom | $M_x$+,$B$−,**P**−, **top** | $M_x$−,**B**+,**P**−, **top** | |
| 0 | 0 | 0 | 0 | 0 |

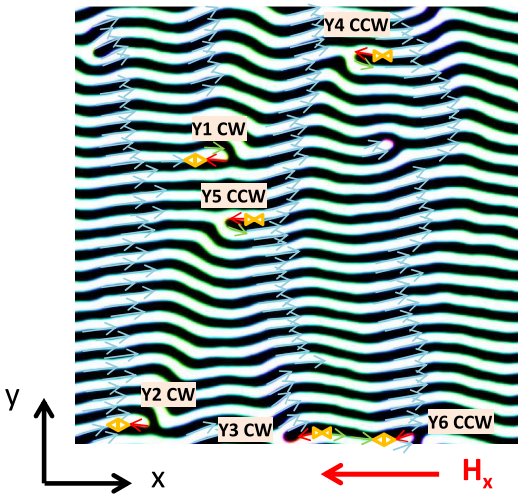


FIG. 8. Micromagnetic simulation of meronlike textures of a 40 nm Nd-Co/30 nm Ni-Fe bilayer under a −17.5 mT field pulse (central plane). White/black stripes correspond to up/down domains ($M_z = \pm M_S$). In-plane magnetization is confined to the domain walls that separate black/white stripes and oriented along them (thin arrows indicate in-plane magnetization at each domain wall). Chirality statistics are balanced in this case (3 CW vs 3 CCW). Note the pronounced zigzags of the stripe pattern. Double arrows indicate Bloch points.

This pronounced separation is based on the disruption, by the stripe domain dislocation cores, of the periodic closure vortex pattern of magnetization in the film which leads to the appearance of small reversed nuclei that cause the observed top/bottom asymmetry. Additionally, we have observed that small magnetic dislocation densities favor opposite meron chiralities at top/bottom surfaces, which may be associated with a symmetry breaking in the propagation of RH/LH Bloch points during meron nucleation. These results are a consequence of the detailed local magnetization symmetries for stray field minimization and, therefore, are of general applicability independent of the chemical composition of the layers. They might pave the way to 3D micromagnetic engineering in future applications.

## ACKNOWLEDGMENTS

This paper was supported by Spanish Ministerio de Economía, y Competitividad (MINECO; Grants No. FIS2013-45469 and No. FIS2016-76058) and by Fundación para el Fomento en Asturias de la Investigación Científica Aplicada y la Tecnología (FICYT-Asturias; Grant No. FC-15-GRUPIN14-040). A.H.-R. acknowledges support from Fundação para a Ciência e a Tecnologia (FCT) of Portugal (Grant No. SFRH/BPD/90471/2012). C.B.-R. appreciates support from CSIC Junta para la Ampliación de Estudios (JAE) Predoc Program. Thanks to R. Valcarcel for technical assistance.

## APPENDIX A: SYMMETRY OPERATIONS AND EQUIVALENCE RELATIONS ON MERONLIKE TEXTURES

Symmetry operations were used to obtain equivalence relations between the different observed meronlike textures. For example, as sketched in Fig. 7(a), a 180° rotation around $\mathbf{u_x}$ that induces a sign change of $y$, $z$, $M_y$, and $M_z$ causes an inversion of polarity and bottom-top sample surfaces which implies that a ($M_x$+,B+,P+) meron texture at the bottom surface is equivalent to a ($M_x$+,B+,P−) meron texture at the top surface. Also, as indicated in Fig. 7(b), a 180° rotation around $\mathbf{u_z}$ causes a sign inversion of Burgers vector, $M_x$, and of the magnetic field $H_x$ applied during meron nucleation so that a ($M_x$+,B+,P+) meron texture nucleated under $-H_x$ is equivalent to a ($M_x$−,B−,P+) meron texture nucleated under $+H_x$. Index transformation upon 180° rotations around $\mathbf{u_x}$ and $\mathbf{u_z}$ have been performed in order to obtain the equivalence criteria between the different possible meron textures, as indicated in Tables III and IV for samples A and B, respectively. This has allowed us to transform the raw experimental statistics of Table I into the simplified Table II shown in this paper.

## APPENDIX B: MICROMAGNETIC SIMULATIONS OF INTERACTING DISLOCATIONS IN NdCo/FeNi BILAYER

Interactions between dislocations can have a clear effect on the nucleation of meronlike textures, particularly in chirality selection, as shown in the micromagnetic simulations of a NdCo/NiFe bilayer (Fig. 8). All meron textures in this simulation emerge at the bottom layer, following the strong selection rule. The dislocation density is relatively large, which creates deformations of the stripe pattern and bends the dislocation axes away from the field direction (note the pronounced zigzags in the stripe pattern shown in Fig. 8). This provides an additional mechanism to break the symmetry between the two branches of the dislocation and select the preferred branch for Bloch point propagation. In this case, the resulting meron texture chirality depends on the local magnetic environment leading to balanced CW/CCW distributions.

[1] M. Y. Im, P. Fischer, K. Yamada, T. Sato, S. Kasai, Y. Nakatani, and T. Ono, Nature Comm. **3**, 983 (2012).
[2] L. Thomas, M. Hayashi, R. Moriya, C. Rettner, and S. Parkin, Nature Comm. **3**, 810 (2012).
[3] A. Huber and R. Schäfer, *Magnetic Domains* (Springer-Verlag, Berlin, Heidelberg, 1998).
[4] S. K. Kim and O. Tchernyshyov, Phys. Rev. B **88**, 174402 (2013).
[5] A. Dussaux, P. Schoenherr, K. Koumpouras, J. Chico, K. Chang, L. Lorenzelli, N. Kanazawa, Y. Tokura, M. Garst, A. Bergman, C. L. Degen, and D. Meier, Nature Comm. **7**, 12430 (2016).
[6] X. Yu, M. Mostovoy, Y. Tokunaga, W. Zhang, K. Kimoto, Y. Matsui, Y. Kaneko, N. Nagaosa, and Y. Tokura, Proc. Nat. Acad. Sci. **109**, 8856 (2012).
[7] U. K. Rossler, A. N. Bogdanov, and C. Pfleiderer, Nature **442**, 797 (2006).

[8] C. Moreau-Luchaire, C. Moutafis, N. Reyren, J. Sampaio, C. A. F. Vaz, N. Van Horne, K. Bouzehouane, K. Garcia, C. Deranlot, P. Warnicke, P. Wohlhüter, J.-M. George, M. Weigand, J. Raabe, V. Cros, and A. Fert, Nature Nanotech. **11**, 444 (2016).
[9] W. Jiang, P. Upadhyaya, W. Zhang, G. Yu, M. B. Jungfleisch, F. Y. Fradin, J. E. Pearson, Y. Tserkovnyak, K. L. Wang, O. Heinonen, S. G. E. te Velthuis, and A. Hoffmann, Science **349**, 283 (2015).
[10] A. Fert, V. Cros, and J. Sampaio, Nature Nanotech. **8**, 152 (2013).
[11] A. Pushp, T. Phung, C. Rettner, B. P. Hughes, S.-H. Yang, L. Thomas, and S. S. P. Parkin, Nature Phys. **9**, 505 (2013).
[12] C. Nam, M. D. Mascaro, and C. A. Ross, Appl. Phys. Lett. **97**, 012505 (2010).
[13] F. Cheynis, A. Masseboeuf, O. Fruchart, N. Rougemaille, J. C. Toussaint, R. Belkhou, P. Bayle-Guillemaud, and A. Marty, Phys. Rev. Lett. **102**, 107201 (2009).
[14] A. Haldar and A. O. Adeyeye, Appl. Phys. Lett. **106**, 032404 (2015).
[15] M. Kammerer, M. Weigand, M. Curcic, M. Noske, M. Sproll, A. Vansteenkiste, B. Van Waeyenberge, H. Stoll, G. Woltersdorf, C. H. Back, and G. Schuetz, Nature Comm. **2**, 279 (2011).
[16] H. Du, R. Che, L. Kong, X. Zhao, C. Jin, C. Wang, J. Yang, W. Ning, R. Li, C. Jin, X. Chen, J. Zang, Y. Zhang, and M. Tian, Nature Comm. **6**, 8504 (2015).
[17] B. F. Miao, L. Sun, Y. W. Wu, X. D. Tao, X. Xiong, Y. Wen, R. X. Cao, P. Wang, D. Wu, Q. F. Zhan, B. You, J. Du, R. W. Li, and H. F. Ding, Phys. Rev. B **90**, 174411 (2014).
[18] D. Gilbert, B. B. Maranville, A. L. Balk, B. J. Kirby, P. Fischer, D. T. Pierce, J. Unguris, J. A. Borchers, and K. Liu, Nature Comm. **6**, 8462 (2015).
[19] J. Li, A. Tan, K. W. Moon, A. Doran, M. A. Marcus, A. T. Young, E. Arenholz, S. Ma, R. F. Yang, C. Hwang, and Z. Q. Qiu, Nature Comm. **5**, 4704 (2014).
[20] R. Lavrijsen, Ji-Hyun Lee, A. Fernández-Pacheco, D. C. M. C. Petit, R. Mansell, and R. P. Cowburn, Nature **493**, 647 (2013).
[21] Y. Y. Dai, H. Wang, P. Tao, T. Yang, W. J. Ren, and Z. D. Zhang, Phys. Rev. B **88**, 054403 (2013).
[22] M. Hänze, C. F. Adolff, B. Schulte, J. Möller, M. Weigand, and G. Meier, Sci. Rep. **6**, 22402 (2016).
[23] O. A. Tretiakov and O. Tchernyshyov, Phys. Rev. B **75**, 012408 (2007); A. Tan, J. Li, A. Scholl, E. Arenholz, A. T. Young, Q. Li, C. Hwang, and Z. Q. Qiu, *ibid.* **94**, 014433 (2016).
[24] Y. Zhou and M. Ezawa, Nature Comm. **5**, 4652 (2014).
[25] M. Ezawa, Phys. Rev. B **83**, 100408(R) (2011).
[26] S. Wintz, C. Bunce, A. Neudert, M. Körner, T. Strache, M. Buhl, A. Erbe, S. Gemming, J. Raabe, C. Quitmann, and J. Fassbender, Phys. Rev. Lett. **110**, 177201 (2013).
[27] M. Pereiro, D. Yudin, J. Chico, C. Etz, O. Eriksson, and A. Bergman, Nature Comm. **5**, 4815 (2014).
[28] C. Blanco-Roldán, C. Quirós, A. Sorrentino, A. Hierro-Rodríguez, L. M. Álvarez Prado, R. Valcárcel, M. Duch, N. Torras, J. Esteve, J. I. Martín, M. Vélez, J. M. Alameda, E. Pereiro, and S. Ferrer, Nature Comm. **6**, 8196 (2015).
[29] S.-Z. Lin, A. Saxena, and C. D. Batista, Phys. Rev. B **91**, 224407 (2015).
[30] C. Blanco-Roldán, Y. Choi, C. Quirós, S. M. Valvidares, R. Zarate, M. Vélez, J. M. Alameda, D. Haskel, and J. I. Martín, Phys. Rev. B **92**, 224433 (2015).
[31] A. Hierro-Rodriguez, R. Cid, M. Vélez, G. Rodriguez-Rodriguez, J. I. Martín, L. M. Álvarez- Prado, and J. M. Alameda, Phys. Rev. Lett. **109**, 117202 (2012).
[32] J. Stohr and H. C. Siegmann, *Magnetism: From Fundamentals to Nanoscale Dynamics* (Springer, Heidelberg, 2006).
[33] E. Pereiro, J. Nicolas, S. Ferrer, and M. R. Howells, J. Synchrotron Rad. **16**, 505 (2009).
[34] A. Sorrentino, J. Nicolás, R. Valcárcel, F. J. Chichón, M. Rosanes, J. Avila, A. Tkachuk, J. Irwin, S. Ferrer, and E. Pereiro, J. Synchrotron Rad. **22**, 1112 (2015).
[35] A. Vansteenkiste, J. Leliaert, M. Dvornik, M. Helsen, F. Garcia-Sanchez, and B. Van Waeyenberge, AIP Advances **4**, 107133 (2014).
[36] G. E. Rowland, Muview, http://www.grahamerowlands.com/main/muview/.
[37] M. Yan, C. Andreas, A. Kákay, F. García-Sánchez, and R. Hertel, Appl. Phys. Lett. **100**, 252401 (2012).